

This manuscript has been submitted to Elementa: Science of the Anthropocene, the special feature of The Multidisciplinary Drifting Observatory for the Study of Arctic Climate (MOSAIC). Please note that, despite having undergone peer-review, this manuscript has yet to be formally accepted for publication. Subsequent versions of this manuscript might have slightly different content. When accepted, the final version of this manuscript will be available via this 'Peer-reviewed Publication DOI' link on the right-hand side of this webpage. Please feel free to contact any of the authors, we welcome all feedback.

1
2
3
4
5
6
7
8
9
10
11
12
13
14
15
16
17
18
19
20

Seasonality of spectral radiative fluxes and optical properties of Arctic sea ice during the spring-summer transition

Ran Tao^{1,2}, Marcel Nicolaus¹, Christian Katlein¹, Philipp Anhaus¹, Mario Hoppmann¹, Gunnar Spreen², Hannah Niehaus², Evelyn Jäkel³, Manfred Wendisch³, and Christian Haas^{1,2}

¹ Alfred-Wegener-Institut Helmholtz-Zentrum für Polar- und Meeresforschung, Bremerhaven, Germany

² University of Bremen, Institute of Environmental Physics, Bremen, Germany

³ Leipzig University, Leipzig Institute for Meteorology, Leipzig, Germany

* corresponding author: Ran Tao (ran.tao@awi.de)

Abstract

The reflection, absorption, and transmittance of solar (shortwave) radiation by sea ice play a crucial role in physical and biological processes in the ice-covered Arctic Ocean and atmosphere. These sea ice optical properties are of great importance, in particular during the melt season, as they significantly impact energy fluxes within and the total energy budget of the coupled atmosphere-ice-ocean system. In this paper, we analyse data from

21 autonomous drifting stations to investigate the seasonal evolution of the spectral albedo,
22 transmittance and absorptivity for different sea ice, snow, and surface conditions as
23 measured during the MOSAiC expedition in 2019-2020. We find that the spatial variability of
24 these quantities was small during spring, and that it strongly increased after the melt onset
25 on May 26, 2020, when the liquid water content on the surface increased. The enhanced
26 variability was then mostly determined by the formation of melt ponds. The formation of a
27 single melt pond can increase the energy absorption of the sea ice by 50% compared to
28 adjacent bare ice sites. The temporal evolution of the surface albedo and the sea ice
29 transmittance was mostly event-driven and, thus, neither continuous nor linear.
30 Furthermore, absorptivity and transmittance showed strong temporal and spatial
31 variabilities, which depended on internal sea ice properties and under-ice biological
32 processes and not only surface conditions. The spatial and temporal heterogeneity of sea ice
33 conditions strongly impacted the partitioning of the solar short-wave radiation. This study
34 shows that the formation and development of melt ponds can reduce albedo to 1/3,
35 enhancing the total (summer) heat deposition. Individual ponding events can lead to more
36 energy deposition than an earlier melt onset. The small-scale heterogeneity and the timing
37 and duration of ponding events have to be considered when comparing (local) in-situ
38 observations with large-scale satellite remote sensing datasets, and can help to improve
39 numerical models.

40

41 Key points

- 42 - The transition of sea ice surface conditions from spring to summer is event-driven
- 43 and neither continuous nor linear
- 44 - The summer energy budget of sea ice is more sensitive to melt pond evolution than
- 45 to melt onset dates
- 46 - The seasonality of absorbed and transmitted radiation is not directly linked to the
- 47 surface evolution
- 48 - The large variability between closely located stations can impact the large scale
- 49 energy budget profoundly

50

51 1. Introduction

52 The surface energy budget of the Arctic summer ice cover is affected significantly by the
53 observed decline of sea ice (e.g., Comiso et al., 2012., Nicolaus et al., 2012). The Arctic Sea
54 ice shows an earlier melt onset and later freeze-up, thus a longer melt season. The small
55 sea ice albedo during this period results in more solar radiative energy being absorbed by
56 the sea ice and the ocean underneath (e.g., Comiso et al., 2012; Serreze and Stroeve, 2015;
57 Stroeve and Notz, 2018). Sea-ice extent is shrinking (Serreze et al., 2015; Stroeve et al.,
58 2014), thickness is decreasing (e.g., Haas et al., 2008; Kwok, 2018), and multi-year ice (MYI)
59 is largely replaced by seasonal first-year ice (FYI) (e.g., Maslanik et al., 2011; Stroeve and
60 Notz, 2018). Concurrently, the near-surface air temperature in the Arctic has increased two
61 to three times more than the corresponding global mean surface temperature (e.g.,
62 Wendisch et al., 2022). The increasing air temperature provides more heat to melt the snow
63 cover, resulting in decreasing albedo. Particularly, the transition from dry to wet snow

64 results in a significant albedo decrease (Nicolaus et al., 2010; Perovich and Polashenski,
65 2012). The spatial and temporal variability of optical properties of the snow and sea ice such
66 as albedo, transmittance and absorptivity increase after melt onset and subsequent melt
67 pond formation (e.g., Perovich et al., 2002).

68 The melting snow increases the light transmittance and the amount of downwelling solar
69 irradiance penetrating through the snow-covered sea ice, which impacts the physical and
70 biological processes underneath the sea ice cover (e.g., Anhaus et al., 2021; Ardyna et al.,
71 2020; Katlein et al., 2019; Perovich et al., 2008; Perovich and Richter-Menge, 2015). On the
72 aggregate scale, approximately 8 % of the incident solar irradiance is transmitted into the
73 ocean underneath in one year (Perovich 2005). The overwhelming amount (approximately
74 96 %) of the annually transmitted solar radiative energy penetrates through the sea ice layer
75 during the four-month period from May to August when a sufficient amount of irradiance
76 can be deposited on the surface with low albedo (Arndt and Nicolaus, 2014; Perovich 2005).

77 A detailed investigation of the temporal evolution and spatial variability of the surface and
78 optical properties is needed to accurately represent the large-scale energy balance of the
79 Arctic sea ice. Here, we present a dataset of spectral albedo and transmittance from 10
80 autonomous radiation measurement stations deployed during the MOSAiC expedition
81 (Multidisciplinary Drifting Observatory for the Study of Arctic Climate) in 2019-2020
82 (Nicolaus et al., 2022). In-situ observations provide a detailed insight into the radiative
83 partitioning in and through sea ice, which is otherwise inaccessible via satellite observation.
84 We focus on the period from April 1 to July 18, 2020, when the Arctic sea ice transitioned
85 from spring to summer. This paper identifies the seasonality and key events during this

86 transition, examines the radiative partitioning during the transition period, and highlights
87 their impact on the larger-scale energy balance.

88 2. Methods

89 2.1. The MOSAiC drift

90 The dataset presented in this study was obtained during the MOSAiC expedition (2019-
91 2020) with the German research ice breaker *Polarstern* (Knust et al., 2017), following the
92 Transpolar Drift (Nicolaus et al., 2022). The drift of *Polarstern* consisted of 3 phases:

93 (1) Drift 1 started in the Central Arctic at 85°N on October 4, 2019 and lasted until
94 May 16, 2020, when *Polarstern* left the floe and paused the manned observation,
95 while autonomous measurements continued.

96 (2) Drift 2 started on the same floe as Drift 1 on June 19, 2020, and lasted until July
97 31, 2020, when the floe disintegrated in the Fram Strait (78.9°N). Subsequently,

98 (3) Drift 3 started on a new floe near the North Pole (87.7°N) on August 21, 2020
99 and followed the Transpolar drift stream until September 20, 2020.

100 During the MOSAiC expedition, altogether 10 autonomous stations were deployed to
101 measure spectral solar radiation fluxes above and under sea ice (Table 1). These radiation
102 stations follow the concept described by Nicolaus et al. (2010b), and Figure 1 shows the drift
103 track of the 10 radiation stations. The majority of the radiation stations (7) were installed
104 during Drift 1 from October 5, 2019, to August 8, 2020, when the autonomous stations were
105 recovered. The data collected during this period provide important observations covering
106 the key spring-summer transition from May 16 to June 19, 2020, when no manned
107 observations were possible due to the absence of *Polarstern* (between Drift 1 and 2).

108 Furthermore, autonomous buoys 2020M29 and 2019S94 provide the evolution of air and
109 surface temperature during the melt season.

110 Table 1. Operational times and metadata of all the autonomous radiation stations
 111 operated during the MOSAiC expedition. The 3 radiation stations in bold (2020R11
 112 at the LM site, 2020R12 at the L3 site, and 2020R14 at the CO1 site) are discussed
 113 in detail in this study.

Station name	Site	Initial snow depth (m)	Initial ice thickness (m)	Deployment	First good data	Last good data	Failure/recovery	Comment
2019R8	L1	0.18	0.78	Oct 05, 2019	Oct 6, 2019	Jun 13, 2020	Aug 06, 2020	Low sun elevation angle and hardware malfunction
2019R9	L2	0.10	0.30	Oct 07, 2019	Mar 13, 2020	Jun 12, 2020	Jun 17, 2020	Data interruption hardware malfunction
2020R10	CO1	0.07	1.49	Mar 08, 2020	Mar 13, 2021	Jul 20, 2020	Jul 21, 2020	Destroyed by ridge activity
2020R11	LM	0.18	1.59	Mar 26, 2020	Mar 29, 2020	Jul 18, 2020	Aug 01, 2020	
2020R12	L3	0.08	1.67	Apr 24, 2020	Apr 24, 2020	Jul 22, 2020	Aug 08, 2020	
2020R13	CO1	0.92	4.28	May 06, 2020	May 6, 2020	May 12, 2020	May 15, 2020	Destroyed by ridge activity
2020R14	CO1	0.12	3.13	Apr 03, 2020	Apr 03, 2020	Jul 15, 2020	Jul 15, 2020	
2020R15	CO2	0.01	1.52	Jul 12, 2020	Jul 13, 2020	Jul 19, 2020	Jul 19, 2020	Data interruption due to hardware malfunction
2020R21	CO3	0.35 (pond depth)	0.59	Aug 27, 2020	Aug 27, 2020	Sept 25, 2020	Nov 14, 2020	Deployed in a melt pond
2020R22	CO3	unknown	1.34	Aug 21, 2020	Aug 21, 2020	Sept 12, 2020	Sep 12, 2020	Data interruption due to hardware malfunction

115 2.2. Radiation station measurements and data processing

116 Each radiation station consisted of 3 RAMSES-ACC-VIS hyperspectral radiometers (TriOS
117 GmbH, Rastede, Germany; Nicolaus et al., 2010b), measuring spectral irradiance from 320
118 nm to 950 nm with a spectral resolution of 3.3 nm. Measurement interval was 10 minutes.
119 Figure 2 shows photos of both the above-ice and under-ice sensors. Above the ice, the
120 upward-looking sensor measured incident (downwelling) irradiance ($E_i(\lambda, t)$) and the
121 downward-looking sensor measured reflected (upwelling) irradiance ($E_u(\lambda, t)$). The sensor
122 installed under the ice measured the transmitted (downwelling) irradiance ($E_d(\lambda, t)$). The
123 under-ice sensor was placed approximately 0.5 m below the ice bottom, measuring the
124 transmitted irradiance through the sea ice, which can be covered with snow, surface
125 scattering layer (bare ice), or liquid water (melt pond). During the observation time, the
126 distance from the under-ice sensor to the ice bottom varied due to sea ice growth/melt.
127 The spectral irradiance above (upwelling and downwelling) and below (downwelling) the
128 sea ice layer was recorded in counts per channel and then calibrated to absolute spectral
129 irradiances (in $W m^{-2} nm^{-1}$) based on individual calibration files for each sensor (Nicolaus et
130 al., 2010). The spectra were interpolated onto a 1 nm grid to calculate the ratios of spectral
131 albedo, $\alpha(\lambda, t)$:

$$132 \quad \alpha(\lambda, t) = E_u(\lambda, t)/E_i(\lambda, t) \quad (1)$$

133 and transmittance, $\tau(\lambda, t)$, as a ratio of E_d to E_i :

$$134 \quad \tau(\lambda, t) = E_d(\lambda, t)/E_i(\lambda, t) \quad (2)$$

135 as a function of wavelength (λ) and time (t).

136 Nicolaus et al. (2010b) found insufficient data quality between 748 and 773 nm due to small
137 E_i values resulting from Oxygen absorption around 760 nm. Hence, the albedo was linearly
138 interpolated within this wavelength range.

139 The wavelength-integrated broadband albedo ($\alpha_T(t)$) and transmittance ($\tau_T(t)$) were
140 calculated within the wavelength range of 350 nm to 920 nm via the following equations:

$$141 \quad \alpha_T(t) = \frac{\int \alpha(\lambda,t)E_i(\lambda,t)d\lambda}{\int E_i(\lambda,t)d\lambda} \quad (3)$$

$$142 \quad \tau_T(t) = \frac{\int \tau(\lambda,t)E_i(\lambda,t)d\lambda}{\int E_i(\lambda,t)d\lambda} \quad (4)$$

143

144 From the wavelength-integrated irradiances, we have calculated the following quantities:

145 (i) Net irradiance entering the sea ice, E_{ice} ,

$$146 \quad E_{ice}(t) = E_i(t) - E_u(t) \quad (5)$$

147 (ii) Irradiance absorbed by the sea ice layer, E_a , and absorptivity, $abs_T(t)$:

$$148 \quad E_a(t) = E_i(t) - E_u(t) - E_d(t) \quad (6)$$

$$149 \quad abs_T(t) = 1 - \alpha_T(t) - \tau_T(t) \quad (7)$$

150 Note that the upward irradiance from the ocean to the sea ice bottom is
151 omitted from the calculation as it may be assumed to be extremely small (ca. 1%)
152 (Smith and Baker, 1981).

153 (iii) Sea ice melt rate (m_{eq}) from the accumulated E_a and E_d over time through the
154 surface and the ice:

155
$$m_{eq} = \frac{Q_A}{L_{melt} \cdot \rho_{ice}} \quad (8)$$

156
$$m_{eq} = \frac{Q_E}{L_{melt} \cdot \rho_{ice}} \quad (9)$$

157 where Q_A and Q_E is the absorbed and transmitted irradiance accumulated over
158 time: $Q_A = \sum E_d \Delta t$ or $Q_E = \sum E_d \Delta t$, assuming the sea ice is at its melting point
159 with a density $\rho_{ice} = 917 \text{ kg m}^{-3}$, and a latent heat of melt $L_{melt} = 0.3335 \text{ J kg}^{-1}$.

160 (iv) Albedo ratio ($\alpha(900)/\alpha(500)$) between the albedo at 900 nm ($\alpha(900)$) and the
161 albedo at 500 nm ($\alpha(500)$). This ratio is sensitive to the liquid water content at the
162 surface, thus an indicator of ponding, due to high absorption of water at 900 nm
163 compared to 500 nm. The albedo ratio decreases from 1 as water accumulates at
164 the surface.

165 (v) Transmittance ratio ($\tau(600)/\tau(450)$) between transmittance at 600 nm ($\tau(600)$) and
166 transmittance at 450 nm ($\tau(450)$). This ratio is sensitive to the Chlorophyll-a
167 content of the ice and upper ocean, and an increase may be used as an indicator
168 for biological activities in or directly underneath sea ice (e.g., Ehn et al., 2008;
169 Perovich et al., 1993).

170 (vi) We derive the wavelength of maximum transmittance of each spectrum as an
171 indicator for the spectral shape that may be associated with biological influences,
172 as used in Nicolaus et al. (2010a).

173 To investigate the long-term seasonality of apparent optical properties (i.e., albedo and
174 transmittance), we used the maximum optical properties with reference to the maximum
175 solar elevation angle. The daily mean irradiance was used to calculate E_d (Equation 5), E_a
176 (Equations 6 and 7). Sub-diurnal variations and synoptic weather events are not resolved in
177 the presented data.

178 2.3. Data quality and uncertainties

179 During the MOSAiC expedition, we deployed 10 autonomous spectral radiation stations on
180 different sea ice and surface conditions. The stations were irregularly checked and
181 maintained, but operated mostly independently. As with other autonomous instruments on
182 drifting sea ice, some stations showed data interruption due to hardware failure (e.g.,
183 sensor or battery fault) or ice dynamics (e.g., ridging event) (as recorded in Table 1).

184 The above-ice radiation sensors were levelled and mounted on the rack, which was secured
185 to the sea ice, a tilt due to the change of the surface or differential settling cannot be
186 avoided during the long-term measurements in the dynamic sea ice regime. Hence, we
187 monitored the inclination angle of the sensor over time, and excluded data with inclination
188 angles larger than 10° . Additionally, we flagged the data as low quality when the solar
189 elevation angle was smaller than 5° . Also, we observed some noise in spectral albedo at
190 wavelength smaller than 400 nm, for the which might be due to the downward-looking
191 sensor. A detailed description of the quality of the sensor and data interpolation, which was
192 adopted in this study, can be found in Nicolaus et al. (2010b). Table 1 shows the operational
193 time of each station and the resulting times with high-quality data.

194 Another uncertainty in this study comes from the distance between the under-ice sensor
195 and the sea ice bottom. The initial set-up of approximately 0.5 m was to prevent sea ice
196 growth from intruding the sensor. Due to the nature of autonomous stations, the distance
197 changed over time with ice growth/melt without sensor depth adjustment. The observed
198 transmitted irradiance included the absorption from the top water layer, resulting in a

199 reduction of 20% to 30% of light transmittance (Nicolaus et al., 2010; Wozniak and Dera,
200 2007).

201 For quality control, we performed radiative transfer simulations for comparison with
202 measured spectrally integrated E_i for all individual radiation stations during the
203 measurement period. The modelling considered only cloudless atmospheric conditions, to
204 avoid uncertainties caused by unknown cloud microphysical and macrophysical properties,
205 which were not available for these remote radiation stations. However, a direct comparison
206 for cloudless days allows (i) to monitor the occurrence of clouds, (ii) to identify potential
207 effects of sensor misalignment in cloudless conditions, and (iii) a validation of the
208 radiometric calibration. Broken cloud conditions can be identified by short-term variations
209 of E_i , while more compact cloud situations lead to a general decrease of E_i compared to the
210 simulations. Misalignment of the sensors can be detected by an asymmetric diurnal
211 variation of E_i . The data were not corrected for this, but excluded from further analysis. In
212 contrast to the cloud effects, uncertainties in the radiometric calibration would lead to
213 systematic shifts in the measured E_i under cloud-free conditions compared to the
214 simulations. However, this was not observed, indicating the stability of the radiometric
215 calibration of the upward-looking sensor.

216 The simulations were performed with the library for radiative transfer routines and
217 programs (libRadtran, Emde et al., 2016; Mayer and Kylling, 2005). As a solver for the
218 radiative transfer equation, the Discrete Ordinate Radiative Transfer solver (DISORT)
219 (Stamnes et al., 2000) was chosen. The extra-terrestrial spectrum was taken from Gueymard
220 (2004). The meteorological input for the simulations was based on standard profiles of trace
221 gas concentrations, air temperature, humidity, and pressure from Anderson et al. (1986).

222 The standard Sub-Arctic atmospheric profile was adapted to observations from radio
223 soundings (Maturilli et al., 2021), which were launched about every six hours from
224 *Polarstern*.

225 3. Results

226 3.1. Overview of surface properties and seasonality

227 Figures 3, 4, and 5 summarize the surface condition and seasonal evolution of optical
228 properties for the observation period from May to mid-July, 2020. Figure 3 provides the
229 time series of the measurements of the 10 radiation stations based on daily measurements
230 at times of the highest solar elevation angle (local solar noon). Figure 4 shows photos of the
231 surface conditions and radiation stations taken by autonomous cameras at the LM and L3
232 sites, and of the Central Observatory (CO) from a panorama camera (Panomax) onboard
233 *Polarstern*. Figure 5 shows hourly values of meteorological parameters and a summary of
234 the surface albedo evolution until the end of July. Figures 6, 7, and 8 show the seasonal
235 evolution of spectral albedo and transmittance.

236 The dataset allows a particularly comprehensive analysis of the radiative fluxes of the Arctic
237 sea ice during the spring-summer transition, a period that aligns with the maximum
238 incoming irradiance. This study focuses on 3 radiation stations sited on multi-year ice (Table
239 1), which are later compared to satellite remote sensing observations. The 3 stations are
240 named after their site of deployment hereinafter: LM, L3, and CO. Radiative fluxes showed
241 an increasing spatial variability after the melt onset, mostly attributable to events (e.g.,
242 ponding and drainage, see Figure 4) which did not persist nor progress over the same time
243 scale. This variability is well expressed in different phases and differences in timing and the

244 sequence of events (similar to those defined by Nicolaus et al. (2010a) and Perovich et al.
245 (2002)) in the different stations (Figures 3 and 4). Overall, we distinguished 3 phases of the
246 sea ice and snow surface evolution when transitioning to the melt season:

247 (a) Phase 1 (before May 26) was characterized by the mostly below-freezing point air
248 temperature (0°) and dry snow coverage at all 3 sites.

249 Melt onset occurred on May 26 (as also derived by Light et al. (2022)), when the air
250 temperature remained above 0°C continuously for several days and snow started to
251 melt on the surface.

252 (b) Phase 2 (May 26 to June 27) showed a strong surface spatial variability across the 3
253 sites due to events (e.g., ponding and drainage) at different times. The radiative
254 fluxes reached their maximum during this phase.

255 (c) Phase 3 (after June 28) was characterized by the formation of a weathered surface
256 layer, known as a scattering layer from the optical perspective. The spatial variability
257 of surface properties between the 3 sites decreased compared to Phase 2.

258

259 3.2. Phase 1: Dry snow surface (before May 26)

260 Figure 5a shows that the air temperature reached the melting point (0°C) for two short
261 intervals in April but regularly and for longer times after May 12. The surfaces of the three
262 sites were covered by dry snow in April, e.g., Figures 4A and 4B.

263 From April 1 to May 25, the mean broadband albedo at all 3 sites was as high as 0.89 with a
264 standard deviation of 0.03. Compared to later phases, the three sites had the most similar
265 optical properties and most homogeneous surface conditions, although sea ice thickness

266 and snow depth ranged from 1.59 m to over 3 m. The spectral albedo was higher than 0.80
267 over the entire wavelength range from 350 to 920 nm (e.g., Figure 7 shows the spectral
268 albedo on May 1 at the LM and L3 sites). The mean albedo ratio was 0.87 (+/- 0.03) (Figure
269 3D).

270 The broadband transmittance was lower than 0.10 for all sites. The shape of spectral
271 transmittance suggested no influence of biological activity centred around 490 nm (Figures
272 3E, 3F, and 8).

273 3.3. Phase 2: Melting snow and melt pond formation (May 26 to June 27)

274 Melt onset was detected on May 26 and snow started to melt on the surface (e.g., Figure
275 3D), as defined in Perovich et al., 2002. During Phase 2, the most prominent feature was the
276 high spatial variability in the optical properties between the different sites. This variability is
277 well expressed in differences in timing and the sequence of ponding events (MP1 at the LM
278 site, MP2 at the L3 site, and MP3 again at the LM site).

279 Overall, the 3 sites showed a decrease in albedo at different scales due to melting snow and
280 melt ponds (Figure 3A). The CO site showed a linearly decreasing broadband albedo and no
281 ponding event. There were three individual ponds (MP1, MP2, MP3) that formed within the
282 fields of view of the E_v sensors at the LM and L3 sites (e.g., Figures 4-E, 4-H, and 4-N). Events
283 such as pond formation and later pond drainage increased the spatial variability of surface
284 conditions during Phase 2. Also, the spectral albedo larger than 500 nm (the albedo ratio)
285 showed a decrease due to the increasing liquid water on the surface (Figure 3D). The
286 transmittance at the LM and L3 sites showed an increase and change in the spectral shape.

287 MP1: First melt pond on L3:

288 The first melt pond formed at L3 immediately after the melt onset (Figure 4E). Over at MP1,
289 broadband albedo decreased to 0.58. The shape of the spectral albedo changed drastically
290 from a rather linear- to a dome-shape, and the spectral albedo at a wavelength larger than
291 500 nm decreased below 0.67 (Figure 7, May 29). This resulted in the albedo ratio
292 decreasing to 0.39. The broadband transmittance peaked at 0.08, and the wavelength of the
293 maximum transmittance increased to 526 nm, compared to 496 nm during Phase 1 (Figure
294 3E).

295 On June 1, a thin new snow layer was observed (Figures 4F and 4G), and the L3 site showed
296 an increase in broadband albedo to 0.87 and a decrease in broadband transmittance to
297 0.010. The shape of spectral transmittance showed a strong change (Figures 3E and 3F). On
298 June 5, the maximum wavelength of transmittance increased to 576 nm, and the
299 transmittance ratio peaked at 31.47, which aligns with the high absorption coefficient of
300 under-ice biomass at wavelength centred around 440 nm (e.g., Lund-Hansen et al., 2015;
301 Perovich et al., 1993). Compared to Phase 1 (May 1), the spectral transmittance on June 5
302 showed 2 strong decreases, each centred around 440 and 670 nm (Figure 8).

303 MP2: Melt pond on LM:

304 From June 5 onwards, mean broadband albedo decreased again with an increasing spatial
305 variability (Figure 3A). The melt pond event (MP2, Figure 4H) at the LM site led to a
306 decrease of its broadband albedo to 0.44. A strong decrease in albedo was found at
307 wavelength larger than 550 nm, resulting in the minimum albedo ratio of 0.22 (Figure 3D).

308 On June 14, a new snow layer increased the broadband albedo at the LM site for a day, and
309 the albedo ratio increased temporally to 0.59.

310 The broadband transmittance at the LM site increased to 0.079. The shape of spectral
311 transmittance showed a stronger variability (Figures 3C, 3E and 3F) after June 14, when the
312 broadband transmittance started to decline from its maximum. For instance, on June 14, the
313 transmittance ratio increased rapidly with the decreasing broadband transmittance and
314 peaked at 16.0 (Figures 3F and 8A).

315 On June 17, the un-ponded L3 site showed a similar shape of spectral transmittance. The
316 change in the shape of spectral transmittance persisted towards June 23, when the
317 maximum wavelength of transmittance peaked at 710 nm, and the transmittance ratio
318 peaked at 421 (Figures 3E and 3F).

319 MP3: Second melt pond on L3:

320 At the L3 site, a ponding event was again observed (e.g., Figure 4N), resulting in a minimum
321 albedo of 0.38 on June 25, after a rapid decrease from 0.70 on June 23. The albedo ratio
322 reached the minimum of 0.22 (e.g., Figure 7A).

323 Broadband transmittance remained lower than 0.012 during the formation of MP3.

324 Compared to MP1 (also at the L3 site), even with the minimum albedo and more light being
325 input into the ponded surface, the transmittance during MP3 was significantly lower than
326 0.080. The L3 site showed an absorptivity as high as 0.61 during MP3, compared to 0.34
327 during MP1. The spectral transmittance showed a similar spectral shape compared to June
328 23, with the maximum wavelength at 707 nm and a transmittance ratio of 77.0 (Figures 3E
329 and 3F).

330 3.4. Phase 3: Advanced melt (after June 28)

331 From June 28 onwards, the 3 sites showed surface drainage and a weathered ice layer,
332 resulting in a broadband albedo to show an increasing temporal consistency, and a more
333 linear decline with less spatial variability (Figure 3C). From June 28 to July 18, the mean
334 broadband albedo from all three sites was 0.69 (+/- 0.05) (Figure 3A). The spectral albedo
335 showed a similar shape during this phase (e.g., Figure 8). The mean albedo ratio (Figure 3D),
336 increased to 0.81 (+/- 0.02) on June 28, and then decreased to 0.73 (+/- 0.02) on July 15.

337 The broadband transmittance showed larger spatial variability, mainly attributed to the
338 formation of a lead in the proximity of the L3 site (Figures 3C and 4T). At the L3 site, the
339 spectral transmittance also showed a stronger change than the other 2 sites (Figure 8): e.g.,
340 two distinctive decreases centred around 440 nm and 670 nm were shown on June 28. On
341 June 30 and July 5, the transmittance ratio at the L3 site showed two peaks at 57.8 and 29.5.
342 At the LM site, the shape of spectral transmittance did not change as strongly, with the
343 transmittance ratio of 0.6 and remained so until July 15 (Figures 3E and 3F).

344

345 Summarising the results of 3 individual time series, we find a general progression from
346 spring to summer conditions with the broadband albedo ranging from 0.38 to 0.97 and
347 transmittance from less than 0.010 to 0.120 across 3 sites. After the melt onset, we find an
348 increasing surface variability from the 3 sites, particularly at the LM and L3 sites (compared
349 to the CO site, which showed only a more linear evolution), driven by ponding events. Under
350 the same atmospheric conditions, the timing and effects of events vary by site. Individual
351 events, such as pond formation and drainage, new snow, and lead formation (e.g., Figure
352 4T), have effects, which lead to the short-term decrease of albedo, and an increase in

353 absorptivity and transmittance. At the same site, the energy partitioning during different
354 ponding events was different. For instance, the transmittance at the L3 site did not increase
355 with the formation of MP3. We also examined the temporal evolution of the spectral albedo
356 and transmittance, and distinguished the radiative fluxes into and through the snow and sea
357 ice surface when the Arctic was transitioning from spring to summer.

358

359 3.5. Seasonality of the surface evolution and surface fluxes

360 Figure 9 shows the daily averaged broadband irradiances (incident, penetrating into the sea
361 ice layer (Equation 5), absorbed by the ice layer (Equation 6), and transmitted through the
362 ice layer) during the transition from spring to summer conditions. Figure 10 shows the daily
363 mean of absorbed and transmitted irradiance of the 3 phases and individual events.

364 Phase 1 was characterized by the high albedo and increasing solar irradiance (e.g., Figures
365 5A and 5B). We computed the accumulated energy being deposited into the sea ice and
366 snow surface (surface influx) during a 31-day period from April 25 to May 25, when all 3
367 sites were recording data. With the mean albedo of 0.89, the daily mean energy entering
368 the snow and sea ice was smaller than 2 MJm^{-2} for all 3 sites. Although Phase 1 showed
369 rather homogenous surface conditions at each site, compared to later phases, the energy
370 budget differed between the sites. For instance, the LM site showed 35.6% (15 MJm^{-2}) more
371 energy deposited into the surface of the L3 site.

372 After melt onset, the highest incident irradiance and surface influxes were observed (Phase
373 2). The 3 sites showed a mean surface influx of $3.7 (+/- 1.1) \text{ MJm}^{-2}$ per day, almost twice as
374 much as Phase 1. The LM site showed the highest surface influx (5 MJm^{-2}), mostly

375 contributed by the 15-day duration of MP2. The L3 and CO sites showed a surface influx of
376 3.2 and 3.1 MJm⁻², respectively. During the ponding event of MP2, the LM site showed a
377 daily surface influx of 7.2 MJm⁻² (Figure 10B), ca. twice that of the L3 site during MP1 and
378 MP3 (3.4 and 3.7 MJm⁻², respectively). As the surface melting progressed and the albedo
379 decreased at all 3 sites, the impact of melt ponds (e.g., MP3) on increasing the surface influx
380 became less. For instance, during the formation of MP3, the L3 site showed a surface influx
381 of 3.7 MJm⁻² per day, while the other 2 unponded sites both showed a mean surface influx
382 of 3.2 MJm⁻².

383 Phase 3 is characterized by the weathered surface layer at the 3 sites after surface drainage.
384 The mean surface influx increased to 4.0 (+/- 0.5) MJm⁻². The surface spatial variability
385 between the 3 sites decreased during this phase. Also, a lead formed within 5 m of the L3
386 station, which increased the irradiance underneath the ice.

387

388 4. Discussion

389 4.1. Seasonality of energy deposition and melt rates

390 After melt onset, the surface influx increased at all sites, but not linearly or regularly. The
391 strong spatial variability resulted from the very patchy surface evolution at the individual
392 sites. During the melt season, absorptivity and transmittance varied between individual
393 events (Sections 3.3. and 3.4.). The energy partitioning between in-ice absorptivity and
394 transmission into the ocean varied significantly, impacting the primary internal ice melt rate.

395 After melt onset, the sea ice received the largest energy deposition, when the total
396 absorbed irradiance by the ice and the top ocean layer was 120 (+/- 30) MJm⁻². Assuming

397 bare ice at its melting point, the total absorbed irradiance during Phase 2 had the potential
398 to melt 45.5 (+/- 11.7) cm of sea ice. The mean transmittance during this phase was 0.015,
399 integrating to a total of 7.4 MJm⁻², a potential bottom melt of 2.8 cm.

400 The L3 site showed a total absorbed energy of 102.0 MJm⁻² and total transmitted energy of
401 5.9 MJm⁻² during the entire Phase 2. MP1 resulted in a total absorbed energy of 12.8 MJm⁻²
402 and transmitted energy of 2.8 MJm⁻². In late June, MP3 resulted in a total absorbed
403 irradiance at the L3 site of 27.7 MJm⁻² and the total transmitted energy only 0.2 MJm⁻².
404 Computing the entire Phase 2 (34 days), the L3 site had the potential for internal and
405 bottom ice melt of 38.7 cm and 2.0 cm, respectively.

406 During the entire Phase 2, the LM site showed the largest absorbed energy of 156.0 MJm⁻²
407 due to the formation of MP2, enough to melt 59.0 cm of ice. The transmitted energy was
408 15.5 MJm⁻², equivalent to 5.9 cm ice melt from the bottom. The ponding event (MP2)
409 accounted for a significant portion of the total absorbed and transmitted energy of 97.0 and
410 9.7 MJm⁻², which had the potential to melt 36.7 cm and 3.7 cm ice internally and from the
411 bottom, respectively.

412 During Phase 3, the 3 sites accumulated a mean absorbed energy of 60.3 MJm⁻², equivalent
413 to a 22.8 cm internal ice melt. The transmitted energy showed a higher variability due to the
414 lead formation near the L3 site (e.g., Figures 4 and 10B). Within 16 days, the L3 site
415 accumulated a transmitted energy of 6.6 MJm⁻², enough to melt 2.5 cm ice.

416 Overall, the LM site by far showed the strongest absorption and ice melt. Although the L3
417 and CO sites showed a similar amount of energy deposition, the bottom melt rate of the L3
418 site was higher than the CO site. Having no ponding event, the CO site experienced a

419 bottom melt rate of an order of magnitude smaller, as its transmittance remained a
420 minimum.

421 4.2. Effects of melt ponds

422 In this study, we examined the energy partitioning of 3 sites with different snow, ice, and
423 surface conditions during the spring-summer transition. Commonly, melt onset was on May
424 26, initiating a phase of strong spatial variability with little temporal consistency. As a result,
425 the energy partitioning showed a strong variability, driven by melt pond formation and
426 drainage at different sites and with different timing.

427 The locations of melt ponds depend on surface topography. Melt ponds from the previous
428 year have the potential to pre-condition the location and size of new melt ponds (Thielke et
429 al., 2022; Webster et al., 2022). However, at the time of installation of the stations, it was
430 not foreseeable if or even when ponds might form in the field of view of the E_v sensor,
431 which has a footprint of only 1 m². As a result, the described optical properties and melt
432 pond evolution is not necessarily representative for a region larger than the field of view of
433 the RAMSES sensors. Having consistent results for the 3 long-term stations, we find the
434 same characteristics during the 3 phases. This is also supported by other stations, e.g.,
435 2020R10 (Figure 3A), also showed a ponding event and minimum albedo observation in mid-
436 June, similar to MP2 at the LM site.

437 The 3 stations in this study were at multi-year ice and representative of similar ice
438 conditions. There was an increasing surface spatial variability over a floe scale, starting in
439 late May. The melt pond fraction increased to over 20% in late June (Webster et al., 2022),
440 followed by a temporary decrease due to drainage. Based on measurements from the 3

441 radiation stations, we defined Phase 3 with a start date in late June. However, the surface
442 drainage was not homogeneous for the entire ice floe. In July, the melt pond fraction
443 increased and reached the maximum (Webster et al., 2022).

444 4.3. Representativeness of radiation station measurements

445 In this study, we focused on 3 stations that succeeded in capturing the spring summer
446 transition in 2020 as planned. They were on multi-year ice. The evolution of the LM and L3
447 sites was strongly impacted by partly abrupt changes in melt pond conditions, and thus
448 strongly event-driven. Compared to this, the CO site showed a rather linear seasonal
449 progression, but also had the thickest ice.

450 However, the result is representative for multi-year ice with similar conditions, not the
451 entire ice floe. We were not able to obtain measurements on thin ice, which melted
452 completely in July. Considering the peak solar irradiance, there would be a large amount of
453 energy deposited into the ice and the ocean via the thin ice when transitioning into the
454 summer. Taking into account the expanding and deepening of melt ponds from mid-June
455 (Webster et al., 2022) and later pond drainage (e.g., Light et al., 2022) over a larger floe-size
456 scale, the surface heterogeneity can impact the energy budget of sea ice during the melt
457 season and can alter the location of sea ice melt.

458 Furthermore, the MOSAiC ice floe showed a thinner ice thickness compared to the
459 surrounding and historical records along the same trajectory (Krumpen et al., 2020;
460 Krumpen et al., 2021). This indicated an earlier melt onset and earlier melt pond formation
461 (Krumpen et al., 2021). Figure 11A shows the melt onset date of the MOSAiC stations to

462 satellite data. Compared to the satellite record, the MOSAiC melt onset showed an early
463 melt onset (May 26) for its latitude (6th percentile).

464 Also, a lead was formed within 5 metres of L3 site in July, which increased the observed
465 transmitted irradiance as the light was scattered horizontally. The surface albedo at the L3
466 site was unaffected. Such event could not represent the pure physical evolution of radiative
467 fluxes of sea ice, but only a single unrepresentative case.

468 This study provides insights of the spectral albedo and transmittance of different sea ice
469 types, which is important to understand the solar partitioning over an aggregate scale. We
470 recommend future work to expand this result to a larger area (e.g., aerial images) to
471 improve sea ice classification, and to extend the observation period. This will require a
472 wider range of ice conditions, in particular including this and melting ice.

473 4.4. Comparison to earlier studies

474 Figure 11 compares the seasonality of melt onset date and albedo of the MOSAiC
475 observation to the Tara and SHEBA expeditions (Nicolaus et al., 2010a; Perovich et al., 2002)
476 as well as with satellite remote sensing data from 1998 to 2020. Having multiple stations,
477 we are able to investigate the seasonality, and more importantly, the scale spatial variability
478 of radiative partitioning during this period.

479 The best comparable dataset is from the Tara expedition (Nicolaus et al., 2010a), which is
480 based on a radiation station with the same set-up and sensors as in this study. The Tara
481 station was deployed on 2 m thick ice and snow and drifted from 88.2°N on April 29 to
482 87.8°N on August 1, 2007. Nicolaus et al. (2010a) derived a melt onset on June 10, 15 days
483 later than during MOSAiC. After the melt onset, the Tara albedo first showed an almost

484 linear decrease until reached its minimum on July 1, and the surface drainage occurred on
485 July 3. The mean surface influx transitioned from 45.5 to 54.5 Wm^{-2} during this period
486 (Nicolaus et al., 2010a). During the according phase (Phase 2) of the MOSAiC observation,
487 the mean surface influx ranged from 35.4 (CO site) to 58.1 Wm^{-2} (LM site). The LM site also
488 showed a higher mean absorbed and transmitted irradiance than the Tara station. The
489 maximum transmittance showed a linear increase at the Tara station, reached its maximum
490 (0.66) on July 1. Compared to the MOSAiC station, the LM and L3 sites showed a higher
491 maximum transmittance at an earlier date, due to melt pond events in late May and mid-
492 June. Overall, the LM and L3 sites showed a similar seasonality to the Tara station, whilst the
493 CO site showed lower solar fluxes as it was on thicker ice.

494 The SHEBA experiment drifted in the Beaufort and Chukchi Seas, from 76°N in April to 78 °N
495 at the end of July 1998 (Perovich et al., 1998). It represents sea ice conditions at lower
496 latitudes 20 years earlier. The SHEBA melt onset was 3 days later, on May 29 (Perovich et al.,
497 2002). We extracted 2 points from its albedo line to show the evolution of a bare ice surface
498 and melt pond. After the melt onset, the albedo showed a steady decrease until June 13,
499 when the albedo started to decrease more strongly with higher spatial variability. With the
500 melt pond darkening, a maximum albedo of 0.18 was reached by the end of July. Beyond
501 that, during the entire extent of the SHEBA observation, the minimum albedo of 0.1 was
502 reached in mid-August (Perovich, 2002). On the other hand, the MOSAiC dataset (e.g., the L3
503 site) showed an increasing surface spatial variability directly after the melt onset date.

504 The MOSAiC data set stands out for having multiple stations that monitor radiative fluxes
505 above and under sea ice of different ice conditions, but with the same atmospheric forcing.
506 As a result, our measurements describe a broader range of radiative fluxes of sea ice than a

507 single time series, highlighting variability. This variability is particularly important when the
508 ice is transitioning into the melt season, with peak solar irradiance, and more energy
509 deposition into the sea ice with a higher spatial variability.

510 5. Conclusions

511 In this study, we present the seasonal evolution of radiation fluxes during the spring-
512 summer transition during the MOSAiC expedition in 2019/2020. They provide spectral
513 radiative fluxes on and through different sea ice, snow, and surface conditions during most
514 of the sunlit period. We focus on the seasonal progression during the spring-summer
515 transition by investigating 3 radiation stations, with a continuous record from April 1 to July
516 18, 2020.

517 With results from multiple stations, we identified 3 phases:

- 518 (i) Phase 1: dry snow surface before melt onset on May 26. The three sites were
519 characterised by high albedo and small radiative net influx with a small spatial
520 variability.
- 521 (ii) Phase 2: melting snow and melt pond formation. After melt onset, the air
522 temperature was positive for several days and melting snow increased the liquid
523 water content at the surface. Phase 2 showed the strongest spatial variability
524 due to ponding events (MP1, MP2, and MP3). Different from the previously
525 defined seasonality (e.g., Nicolaus et al., 2010a; Perovich et al., 2002), which
526 separated 'melting snow' and 'melt pond formation'. Phase 2 showed a mixture
527 of surface evolution of reoccurring ponding events (e.g., L3 site) and melting
528 snow over sea ice (e.g., CO site). The evolution of net surface influx during Phase

529 2 was mostly event-driven and neither linear nor continuous. Ponding events
530 might not directly increase light transmittance but absorptivity.

531 (iii) Phase 3: after melt pond drainage on June 29. The three sites showed a steadily
532 decreasing albedo and less variability in the absorptance of the radiative fluxes.
533 However, the transmitted irradiance at the L3 site peaked due to the lead
534 formation in its proximity, which enhanced the bottom melt rate by an order of
535 magnitude compared to Phase 2.

536 Having multiple observation stations, we are able to investigate the solar partitioning of
537 different ice surface conditions. We found that the summer energy budget of sea ice
538 depends more on melt pond evolution than on melt onset dates. For instance, a single
539 ponding event (e.g., MP2) accounted for as high surface influx than the unponded CO site
540 during the entire Phase 2. The strong spatial variability between different ice types and
541 surface conditions can impact the large-scale energy budget.

542 The time series shows strong spatial and temporal variations. On the spatial scales of
543 kilometres, as used for general circulation models (GCM) or satellites, melt onset is usually
544 defined as one specific date for the area. Our radiation stations show that the earliest
545 detected melt is not a good predictor for the large-scale melt onset and that locations with
546 the longest melting season (in our case L3) are not necessarily experiencing the strongest
547 accumulated net surface flux and ice melt over the season (which in our case was the LM
548 site). Therefore, the high spatial and temporal variability we found needs to be taken into
549 account when interpreting larger scale Arctic-wide datasets.

550

551 Data availability

552 The MOSAiC radiation stations data are available on Pangaea (Tao et al.,
553 2022, <https://doi.pangaea.de/10.1594/PANGAEA.949556>). The ice mass balance station
554 2020M29 can be accessed on <https://data.meereisportal.de>, and the Snow Buoy 2019S94
555 is published on Pangaea (Nicolaus et al.,
556 2020, <https://doi.org/10.1594/PANGAEA.925325>).

557

558 Acknowledgements

559 This work was carried out, and data used in this manuscript were produced as part of the
560 international Multidisciplinary drifting Observatory for the Study of the Arctic Climate
561 (MOSAiC) with the tag MOSAiC20192020. We thank all persons involved in the expedition of
562 the research vessel Polarstern during MOSAiC in 2019–2020 (AWI_PS122_00) as listed in
563 Nixdorf et al. (2021). We highly acknowledge the contribution by Ilkka Matero, Julia
564 Regnery, Jan Rohde, Jakob Belter, Steven Fons, Igor Sheikin, Alexey Niubom, David Clemens-
565 Sewall for deploying and/or recovering the radiation stations.

566

567 Funding

568 This work was funded by the German Federal Ministry of Education and Research (BMBF)
569 through financing the Alfred-Wegener-Institut Helmholtz-Zentrum für Polar- und
570 Meeresforschung (AWI) and the Polarstern expedition PS122 under the grant N-2014-H-
571 060_Dethloff, the AWI through its projects: AWI_ROV, AWI_ICE, and AWI_SNOW. The AWI
572 buoy program was funded by the Helmholtz strategic investment Frontiers in Arctic Marine
573 Monitoring (FRAM).

574 R.T. was funded by the Deutsche Forschungsgemeinschaft (DFG, German Research
575 Foundation) – Project-ID 268020496 – through the Transregional Collaborative Research
576 Centre TRR-172 “Arctic Amplification: Climate Relevant Atmospheric and Surface Processes,
577 and Feedback Mechanisms (AC)³”.

578 P.A. was funded through the Alfred-Wegener-Institutes internal project AWI_ROV, through
579 the German Ministry of Education and Research (BMBF) project MOSAiC 3 - IceScan
580 (03F0916A), and additional funds through the project DiatomARCTIC (03F0810A), part of the
581 Changing Arctic Ocean Programme, jointly funded by the UKRI Natural Environment
582 Research Council (NERC) and the BMBF.

583

584 References

585 Anderson, M., A. C. Bliss, and S. Drobot. 2019. Snow Melt Onset Over Arctic Sea Ice from
586 SMMR and SSM/I-SSMIS Brightness Temperatures, Version 4. [Indicate subset used].
587 Boulder, Colorado USA. NASA National Snow and Ice Data Center Distributed Active Archive
588 Center. <https://doi.org/10.5067/A9YK15H5EBHK>. [Date Accessed].

589 Anderson, G., Clough, S., Kneizys, F., Chetwynd, J., and Shettle, E.: AFGL atmospheric
590 constituent profiles (0-120 km), Tech. Rep. AFGL-TR-86-0110, Air Force Geophys. Lab.,
591 Hanscom Air Force Base, Bedford, Mass., 1986.

592 Anhaus P, Katlein C, Nicolaus M, Arndt S, Jutila A and Haas C (2021) Snow Depth Retrieval
593 on Arctic Sea Ice Using Under-Ice Hyperspectral Radiation Measurements. *Front. Earth Sci.*
594 9:711306. doi: 10.3389/feart.2021.711306

595 Ardyna, M., Mundy, C.J., Mayot, N., Matthes, L.C., Oziel, L., Horvat, C., Leu, E., Assmy, P.,
596 Hill, V., Matrai, P.A., Gale, M., Melnikov, I.A. and Arrigo, K.R. (2020). Under-Ice

597 Phytoplankton Blooms: Shedding Light on the 'Invisible' Part of Arctic Primary Production.
598 *Frontiers in Marine Science*, 7. doi:10.3389/fmars.2020.608032.

599 Arndt, S. and Nicolaus, M. (2014). Seasonal cycle and long-term trend of solar energy fluxes
600 through Arctic sea ice. *The Cryosphere*, 8(6), pp.2219–2233. doi:10.5194/tc-8-2219-2014.

601 Comiso, J.C. (2012). Large Decadal Decline of the Arctic Multiyear Ice Cover. *Journal of*
602 *Climate*, 25(4), pp.1176–1193. doi:10.1175/jcli-d-11-00113.1.

603 Ehn, J.K., Mundy, C.J. and Barber, D.G. (2008). Bio-optical and structural properties inferred
604 from irradiance measurements within the bottommost layers in an Arctic landfast sea ice
605 cover. *Journal of Geophysical Research*, 113(C3). doi:10.1029/2007jc004194.

606 Emde, C., Buras-Schnell, R., Kylling, A., Mayer, B., Gasteiger, J., Hamann, U., Kylling, J.,
607 Richter, B., Pause, C., Dowling, T. and Bugliaro, L. (2016). The libRadtran software package
608 for radiative transfer calculations (version 2.0.1). *Geoscientific Model Development*, 9(5),
609 pp.1647–1672. doi:10.5194/gmd-9-1647-2016.

610 Gueymard, C.A. (2004). The sun's total and spectral irradiance for solar energy applications
611 and solar radiation models. *Solar Energy*, 76(4), pp.423–453.
612 doi:10.1016/j.solener.2003.08.039.

613 Haas, C., Pfaffling, A., Hendricks, S., Rabenstein, L., Etienne, J.-L. and Rigor, I. (2008).
614 Reduced ice thickness in Arctic Transpolar Drift favors rapid ice retreat. *Geophysical*
615 *Research Letters*, 35(17). doi:10.1029/2008gl034457.

616 Katlein, C., Arndt, S., Belter, H.J., Castellani, G. and Nicolaus, M. (2019). Seasonal Evolution
617 of Light Transmission Distributions Through Arctic Sea Ice. *Journal of Geophysical Research:*
618 *Oceans*, 124(8), pp.5418–5435. doi:10.1029/2018jc014833.

619 Knust, Rainer (2017). Polar Research and Supply Vessel POLARSTERN operated by the Alfred-
620 Wegener-Institute. *Journal of large-scale research facilities JLSRF* 3.
621 <https://doi.org/10.17815/jlsrf-3-163>.

622 Krumpfen, Thomas, Florent Birrien, Frank Kauker, Thomas Rackow, Luisa von Albedyll,
623 Michael Angelopoulos, H. Jakob Belter, et al. 2020. ‘The MOSAiC Ice Floe: Sediment-Laden
624 Survivor from the Siberian Shelf’. *The Cryosphere* 14 (7): 2173–87.
625 <https://doi.org/10.5194/tc-14-2173-2020>.

626 Krumpfen, Thomas, Luisa von Albedyll, Helge F. Goessling, Stefan Hendricks, Bennet Juhls,
627 Gunnar Spreen, Sascha Willmes, et al. 2021. ‘MOSAiC Drift Expedition from October 2019 to
628 July 2020: Sea Ice Conditions from Space and Comparison with Previous Years’. *The*
629 *Cryosphere* 15 (8): 3897–3920. <https://doi.org/10.5194/tc-15-3897-2021>.

630

631 Kwok, R. (2018). Arctic sea ice thickness, volume, and multiyear ice coverage: losses and
632 coupled variability (1958–2018). *Environmental Research Letters*, 13(10), p.105005.
633 doi:10.1088/1748-9326/aae3ec.

634 Lund-Hansen L. C., Markager S., Hancke K., Stratmann T., Rysgaard S., Ramløv H., & Sorrell B. K. (2015).
635 Effects of sea-ice light attenuation and CDOM absorption in the water below the Eurasian sector of
636 central Arctic Ocean (>88°N). *Polar Research*, 34. <https://doi.org/10.3402/polar.v34.23978>

637 Maslanik, J., Stroeve, J., Fowler, C. and Emery, W. (2011). Distribution and trends in Arctic
638 sea ice age through spring 2011. *Geophysical Research Letters*, 38(13), p.n/a-n/a.
639 doi:10.1029/2011gl047735.

640 Maturilli, M., Holdridge, D.J., Dahlke, S., Graeser, J., Sommerfeld, A., Jaiser, R., Deckelmann,
641 H., Schulz, A., 2021. Initial radiosonde data from 2019-10 to 2020-09 during project MOSAiC,

642 Alfred Wegener Institute, Helmholtz Centre for Polar and Marine Research, Bremerhaven.

643 PANGAEA. <https://doi.org/10.1594/PANGAEA.928656>

644 Mayer, B. and Kylling, A. (2005). Technical note: The libRadtran software package for
645 radiative transfer calculations - description and examples of use. *Atmospheric Chemistry and*
646 *Physics*, 5(7), pp.1855–1877. doi:10.5194/acp-5-1855-2005.

647 Nicolaus, M., Gerland, S., Hudson, S.R., Hanson, S., Haapala, J. and Perovich, D.K. (2010a).
648 Seasonality of spectral albedo and transmittance as observed in the Arctic Transpolar Drift
649 in 2007. *Journal of Geophysical Research*, 115(C11). doi:10.1029/2009jc006074.

650 Nicolaus, M., Hoppmann, M., Lei, R., Belter, H. J., Fang, Y.C., and Rohde, J. (2020): Snow
651 height on sea ice, meteorological conditions and drift of sea ice from autonomous
652 measurements from buoy 2019S94, deployed during MOSAiC 2019/20. Alfred Wegener
653 Institute, Helmholtz Centre for Polar and Marine Research, Bremerhaven,
654 PANGAEA, <https://doi.org/10.1594/PANGAEA.925325>

655 Nicolaus, M., Hudson, S.R., Gerland, S. and Munderloh, K. (2010b). A modern concept for
656 autonomous and continuous measurements of spectral albedo and transmittance of sea ice.
657 *Cold Regions Science and Technology*, 62(1), pp.14–28.
658 doi:10.1016/j.coldregions.2010.03.001.

659 Nicolaus, M., Katlein, C., Maslanik, J. and Hendricks, S. (2012). Changes in Arctic sea ice
660 result in increasing light transmittance and absorption. *Geophysical Research Letters*,
661 39(24). doi:10.1029/2012gl053738.

662 Nicolaus, M., Perovich, D.K., Spreen, G., Granskog, M.A., von Albedyll, L., Angelopoulos, M.,
663 Anhaus, P., Arndt, S., Belter, H.J., Bessonov, V., Birnbaum, G., Brauchle, J., Calmer, R.,
664 Cardellach, E., Cheng, B., Clemens-Sewall, D., Dadic, R., Damm, E., de Boer, G. and Demir, O.
665 (2022). Overview of the MOSAiC expedition: Snow and sea ice. *Elementa: Science of the*
666 *Anthropocene*, 10(1). doi:10.1525/elementa.2021.000046.

667 Perovich, D.K. (2005). On the aggregate-scale partitioning of solar radiation in Arctic sea ice
668 during the Surface Heat Budget of the Arctic Ocean (SHEBA) field experiment. *Journal of*
669 *Geophysical Research: Oceans*, 110(C3). doi:10.1029/2004jc002512.

670 Perovich, D.K., Cota, G.F., Maykut, G.A. and Grenfell, T.C. (1993). Bio-optical observations of
671 first-year Arctic sea ice. *Geophysical Research Letters*, 20(11), pp.1059–1062.
672 doi:10.1029/93gl01316.

673 Perovich, D.K. and Elder, B. (2002). Estimates of ocean heat flux at SHEBA. *Geophysical*
674 *Research Letters*, 29(9), pp.58–158–4. doi:10.1029/2001gl014171.

675 Perovich, D.K. and Polashenski, C. (2012). Albedo evolution of seasonal Arctic sea ice.
676 *Geophysical Research Letters*, 39(8), p.n/a-n/a. doi:10.1029/2012gl051432.

677 Perovich, D.K. and Richter-Menge, J.A. (2015). Regional variability in sea ice melt in a
678 changing Arctic. *Philosophical Transactions of the Royal Society A: Mathematical, Physical*
679 *and Engineering Sciences*, 373(2045), p.20140165. doi:10.1098/rsta.2014.0165.

680 Perovich, D.K., Richter-Menge, J.A., Jones, K.F. and Light, B. (2008). Sunlight, water, and ice:
681 Extreme Arctic sea ice melt during the summer of 2007. *Geophysical Research Letters*,
682 35(11). doi:10.1029/2008gl034007.

683 Perovich, D.K., Roesler, C.S. and Pegau, W.S. (1998). Variability in Arctic sea ice optical
684 properties. *Journal of Geophysical Research: Oceans*, 103(C1), pp.1193–1208.
685 doi:10.1029/97jc01614.

686 Serreze, M.C. and Stroeve, J. (2015). Arctic sea ice trends, variability and implications for
687 seasonal ice forecasting. *Philosophical Transactions of the Royal Society A: Mathematical,*
688 *Physical and Engineering Sciences*, 373(2045), p.20140159. doi:10.1098/rsta.2014.0159.

689 Smith, R.C., and Baker, K.S., "Optical properties of the clearest natural waters (200–800
690 nm)," *Appl. Opt.* 20, 177-184 (1981), <https://doi.org/10.1364/AO.20.000177>

691 Stamnes, K., Tsay, S.-C., Wiscombe, W., and Laszlo, I.: DISORT, A General-Purpose Fortran
692 Program for Discrete-Ordinate-Method Radiative Transfer in Scattering and Emitting
693 Layered Media: Documentation of Methodology, Tech. Rep., Dept. of Physics and
694 Engineering Physics, Stevens Institute of Technology, Hoboken, NJ 07030, 2000.

695 Stroeve, J. and Notz, D. (2018). Changing state of Arctic sea ice across all seasons.
696 *Environmental Research Letters*, 13(10), p.103001. doi:10.1088/1748-9326/aade56.

697 Stroeve, J.C., Markus, T., Boisvert, L., Miller, J. and Barrett, A. (2014). Changes in Arctic melt
698 season and implications for sea ice loss. *Geophysical Research Letters*, 41(4), pp.1216–1225.
699 doi:10.1002/2013gl058951.

700 Tao, R., Anhaus, P., Arndt, S., Belter, H.J., Hoppmann, M., Katlein, C., Matero, I., Regnery, J.,
701 Rohde, J., and Nicolaus, M. (2022). Spectral radiation fluxes, albedo and transmittance
702 from autonomous measurements, deployed during MOSAiC 2019/20. Alfred Wegener
703 Institute, Helmholtz Centre for Polar and Marine Research, Bremerhaven,
704 PANGAEA, <https://doi.org/10.1594/PANGAEA.949556> (in review)

705 Thielke, L., Fuchs, N., Spreen, G., Tremblay, B., Birnbaum, G., Huntemann, M., Hutter, N.,
706 Itkin, P., Jutila, A. and Webster, M.A. (2022). Seasonal predictability of summer melt ponds
707 from winter sea ice surface temperature. doi:10.1002/essoar.10512617.1.

708 Webster, M.A., Holland, M., Wright, N.C., Hendricks, S., Hutter, N., Itkin, P., Light, B.,
709 Linhardt, F., Perovich, D.K., Raphael, I.A., Smith, M.M., von Albedyll, L. and Zhang, J. (2022).
710 Spatiotemporal evolution of melt ponds on Arctic sea ice. *Elementa: Science of the*
711 *Anthropocene*, 10(1). doi:10.1525/elementa.2021.000072.

712 Wendisch, M., M. Brückner, S. Crewell, A. Ehrlich, J. Notholt, C. Lüpkes, A. Macke, J. P.
713 Burrows, A. Rinke, J. Quaas, M. Maturilli, V. Schemann, M. D. Shupe, E. F. Akansu, C.
714 Barrientos-Velasco, K. Bärfuss, A.-M. Blechschmidt, K. Block, I. Bougoudis, H. Bozem,
715 C. Böckmann, A. Bracher, H. Bresson, L. Bretschneider, M. Buschmann, D. G. Chechin,
716 J. Chylik, S. Dahlke, H. Deneke, K. Dethloff, T. Donth, W. Dorn, R. Dupuy, K. Ebell, U.
717 Egerer, R. Engelmann, O. Eppers, R. Gerdes, R. Gierens, I. V. Gorodetskaya, M.
718 Gottschalk, H. Griesche, V. M. Gryanik, D. Handorf, B. Harm-Altstädter, J. Hartmann, M.
719 Hartmann, B. Heinold, A. Herber, H. Herrmann, G. Heygster, I. Höschel, Z. Hofmann, J.
720 Hölemann, A. Hünenbein, S. Jafariserajehlou, E. Jäkel, C. Jacobi, M. Janout, F. Jansen,
721 O. Jourdan, Z. Jurányi, H. Kalesse-Los, T. Kanzow, R. Käthner, L. L. Kliesch, M.
722 Klingebiel, E. M. Knudsen, T. Kovács, W. Körtke, D. Krampe, J. Kretzschmar, D.
723 Kreyling, B. Kulla, D. Kunkel, A. Lampert, M. Lauer, L. Lelli, A. von Lerber, O. Linke, U.
724 Löhnert, M. Lonardi, S. N. Losa, M. Losch, M. Maahn, M. Mech, L. Mei, S. Mertes, E.
725 Metzner, D. Mewes, J. Michaelis, G. Mioche, M. Moser, K. Nakoudi, R. Neggers, R.
726 Neuber, T. Nomokonova, J. Oelker, I. Papakonstantinou-Presvelou, F. Pätzold, V.
727 Pefanis, C. Pohl, M. van Pinxteren, A. Radovan, M. Rhein, M. Rex, A. Richter, N. Risse,
728 C. Ritter, P. Rostosky, V. V. Rozanov, E. Ruiz Donoso, P. Saavedra-Garfias, M.
729 Salzmann, J. Schacht, M. Schäfer, J. Schneider, N. Schnierstein, P. Seifert, S. Seo, H.
730 Siebert, M. A. Soppa, G. Spreen, I. S. Stachlewska, J. Stapf, F. Stratmann, I. Tegen, C.
731 Viceto, C. Voigt, M. Vountas, A. Walbröl, M. Walter, B. Wehner, H. Wex, S. Willmes, M.
732 Zanatta, and S. Zeppenfeld, **2023**: Atmospheric and Surface Processes, and Feedback
733 Mechanisms Determining Arctic Amplification: A Review of First Results and Prospects
734 of the (AC)³ Project, *Bull. Amer. Meteorol. Soc.*, **104 (1)**, **E208–**
735 **E242**, <https://doi.org/10.1175/BAMS-D-21-0218.1>
736
737 Wendisch, M., Müller, D., Schell, D. and Heintzenberg, J. (2001). An Airborne Spectral
738 Albedometer with Active Horizontal Stabilization. *Journal of Atmospheric and Oceanic*
739 *Technology*, 18(11), pp.1856–1866. doi:10.1175/1520-
740 0426(2001)018<1856:aasawa>2.0.co;2.

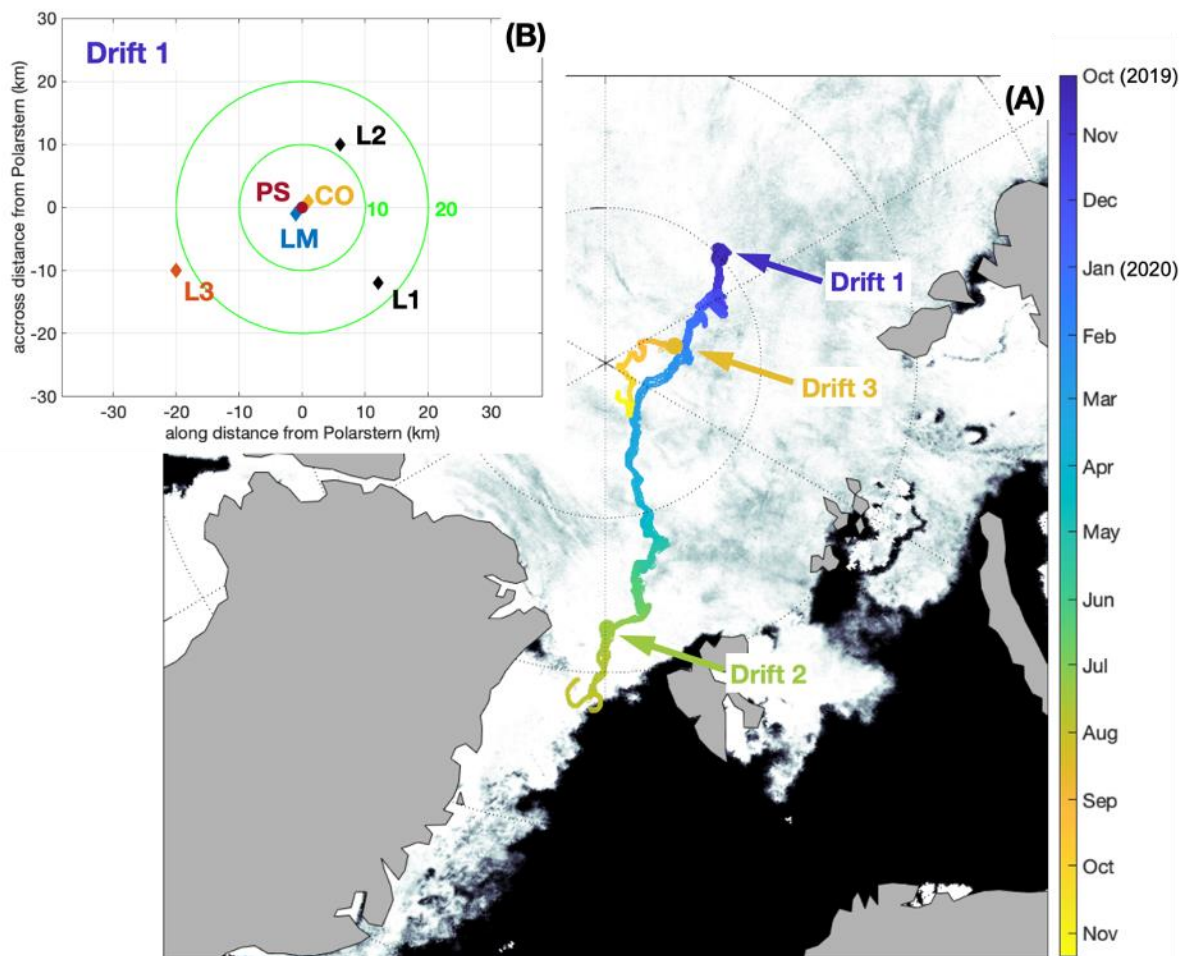
741 Wozniak, B. and Dera, J. (2007). *Light Absorption in Sea Water*. Springer Science & Business

742 Media.

743

744 Figures

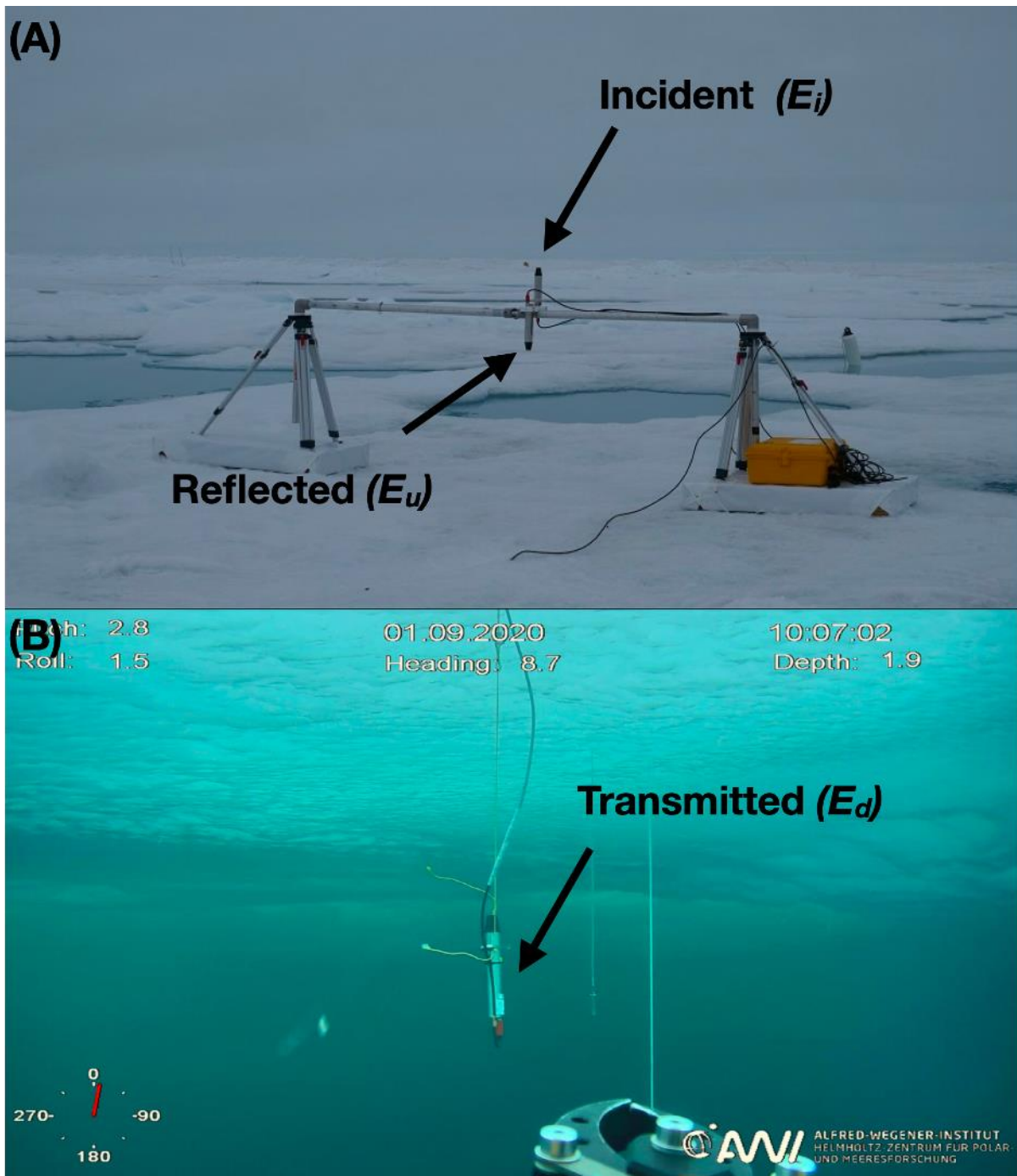
745



746

747 Figure 1. Drift tracks, distribution of sites, and sea ice concentration. (A) Drift tracks
748 of the radiation stations from October 2019 to November 2020. The starting point of
749 Drift 1, 2 and 3 are labelled accordingly. The background shows the sea ice
750 concentration retrieved via AMSR2 (Advanced Microwave Scanning Radiometer 2)
751 on May 25, 2020. (B) Relative positions of the Distributed Network sites (L1, L2, L3,
752 LM) at the beginning of Drift 1, centered around *Polarstern* (PS) and the Central
753 Observatory (CO).

754

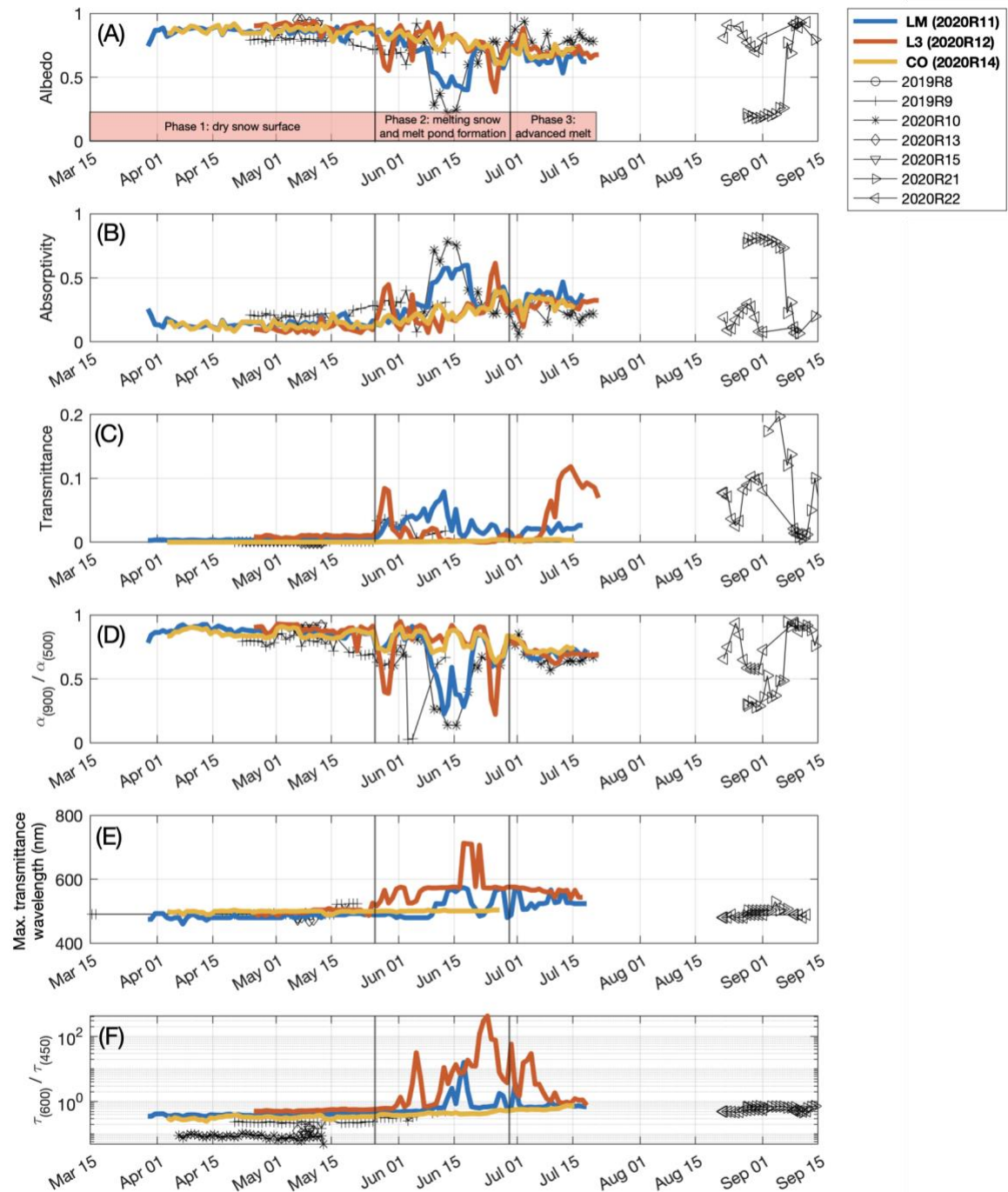


755

756 Figure 2. Photos of a radiation station set-up on and under sea ice. (A) Photograph
 757 of station 2020R15 on July 18, 2020, including the sensors for incident and reflected
 758 irradiance, (B) photograph of station 2020R21 on September 01, 2020, showing the
 759 sensor for transmitted irradiance hanging under the ice. The photo was taken from a
 760 Remotely Operated Vehicle. Labels give attitude parameters of the vehicle.

761

762



763

764 Figure 3. The seasonal progression of optical properties measured by radiation
 765 stations during the sunlit season in 2020. Lines show wavelength-integrated (350-
 766 920 nm) values of (A) surface albedo, (B) surface and ocean absorptivity, (C)
 767 transmittance, (D) Albedo ratio of 900 to 500 nm ($\alpha(900)/\alpha(500)$), (E) Wavelength of
 768 the maximum transmittance of each spectrum, and (F) Transmittance ratio at 600 to

769 450 nm ($\tau(600)/\tau(450)$). The three main radiation stations are highlighted in color:
770 2020R11 at the LM site, 2020R12 at the L3 site, and 2020R14 at the CO site. The
771 two black vertical lines indicated the melt onset (May 26) and stage of advanced melt
772 and the formation of surface weathered layer (June 28).

Phase 1: Dry snow surface

(A) LM site, Apr 14



(B) L3 site, Apr 26



(C) Panomax, Apr 14



Phase 2, first melt pond event (L3 site, MP1)

(D) LM site, May 29



(E) L3 site, May 29: melt pond (MP1)



(F) LM site, June 1: new snow



(G) L3 site, June 1: new snow



Phase 2, melt pond event (LM site, MP2)

(H) LM site, June 12: melt pond (MP2)



(I) L3 site, June 12



(J) LM site, June 20: MP2 drainage



(K) L3 site, June 20



(L) Panomax, Jun 20



Phase 2, second melt pond event (L3 site, MP3)

(M) LM site, Jun 25



(N) L3 site, Jun 25: melt pond (MP3)



(O) Panomax, Jun 25



774

Phase 3, advanced melt

(P) LM site, Jul 1



(Q) L3 site, Jul 1



(R) Panomax, Jul 1



(S) LM Station, Jul 15



(T) L3 site, Jul 15: Lead



(U) Panomax, Jul 15

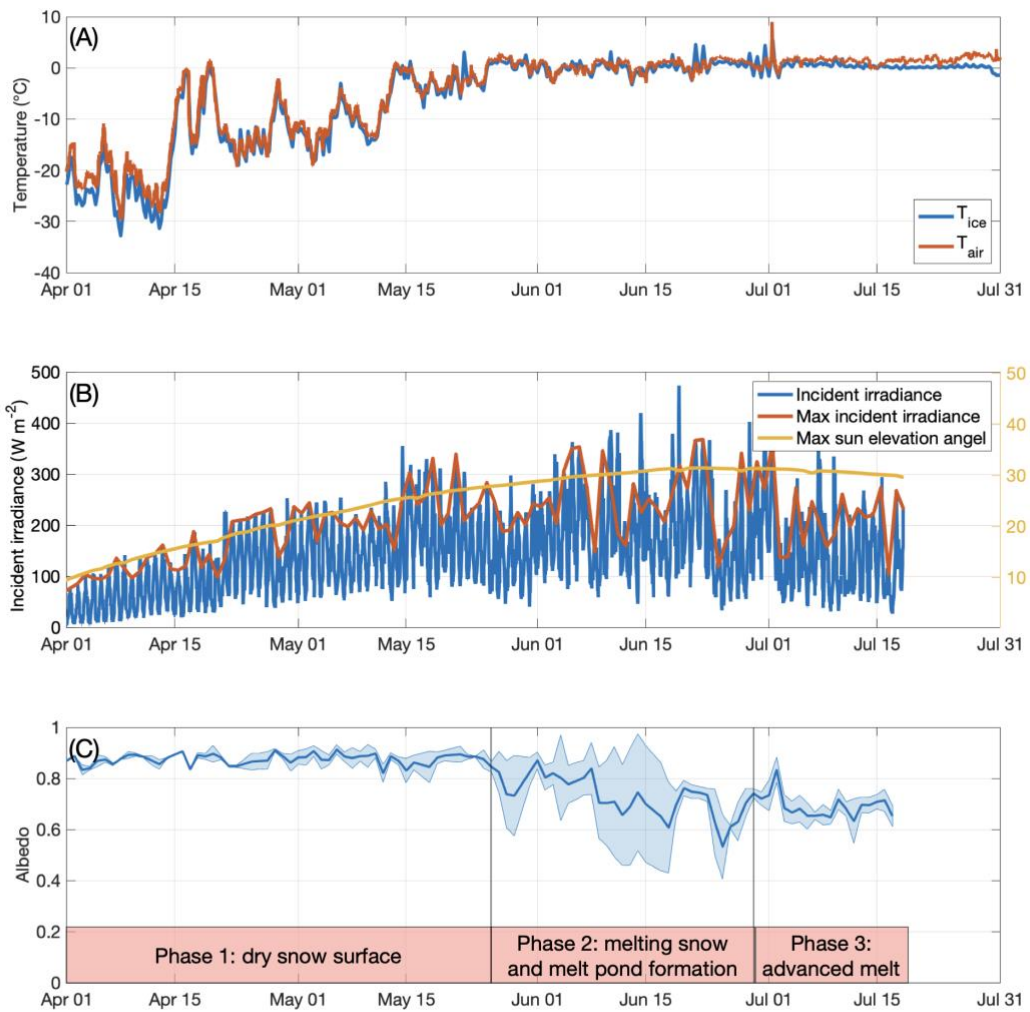


775

776 Figure 4. Surface conditions from April to July, 2020. Photos were taken by
777 autonomous cameras at the LM and L3 site and from *Polarstern* (Panomax camera)
778 monitoring the conditions of and around the radiation stations as labelled with the
779 dates. Note that no photos from *Polarstern* are available for times when the vessel
780 had to leave the floe for logistical reasons.

781

782



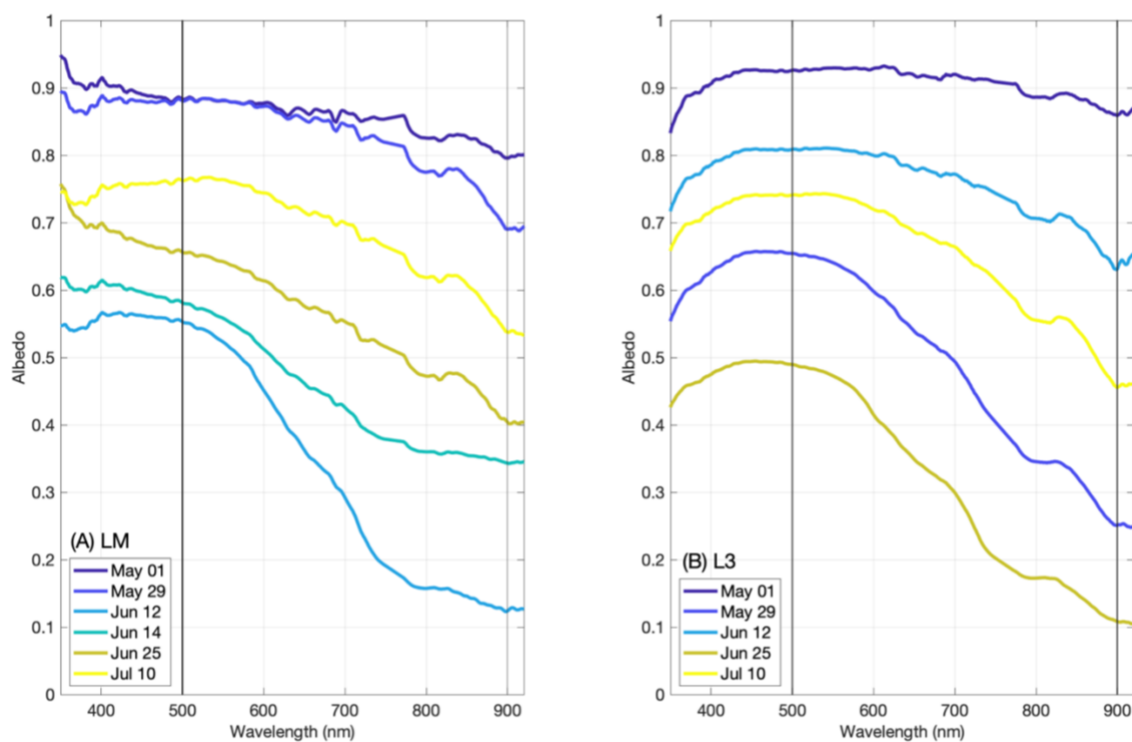
783

784 Figure 5. Surface evolution from April to July 2020. (A) Air and sea ice temperature
 785 from 2020M29 and 2019S94. (B) Incident solar irradiance from 2020R11. (C) Mean
 786 and standard deviation of total albedo from the 3 radiation stations at the LM, L3,
 787 and CO sites (2020R11, 2020R12, and 2020R14). The red-shaded areas mark the
 788 three phases.

789

791 Figure 6. Spectral albedo and transmittance of sea ice from 3 stations in
 792 spring/summer 2020. One spectrum is shown per day, from the measurement at the
 793 time of highest solar elevation. Results for each site are shown on two plates, one for
 794 spectral albedo (α) and one for spectral transmittance (τ) at (A+B) LM, (C+D) L3, and
 795 (E+F) CO. Note the different scale of transmittance for plate F.

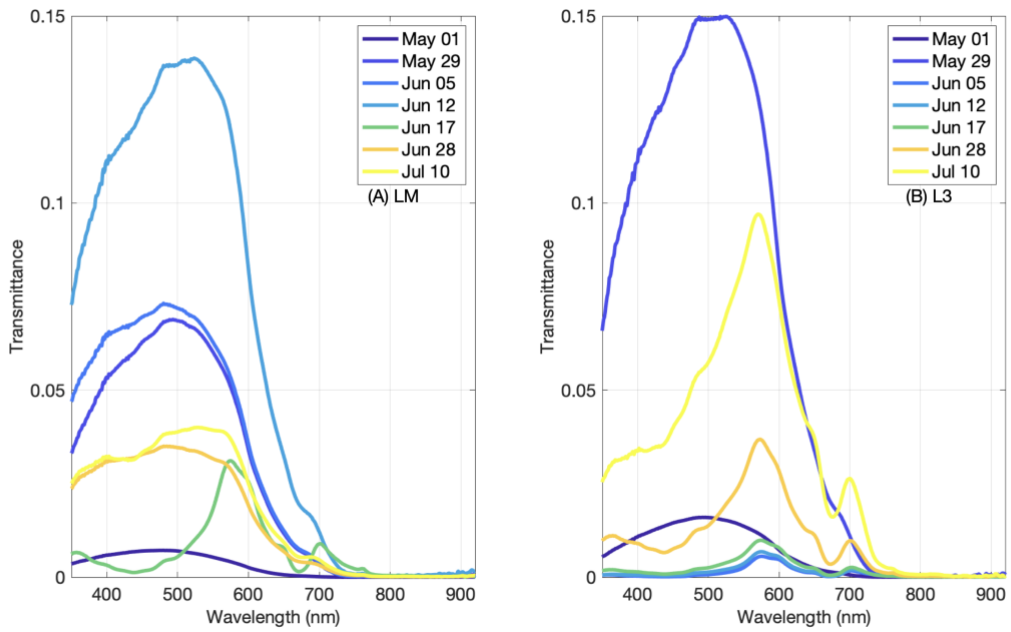
796



797

798 Figure 7. Albedo spectra for selected dates in spring/summer 2020. (A) LM and (B) L3
 799 station. The solid vertical lines highlight the wavelengths of 500 nm and 900 nm, because of
 800 their relevance for the $\alpha(900)/\alpha(500)$ ratio (Figure 4D).

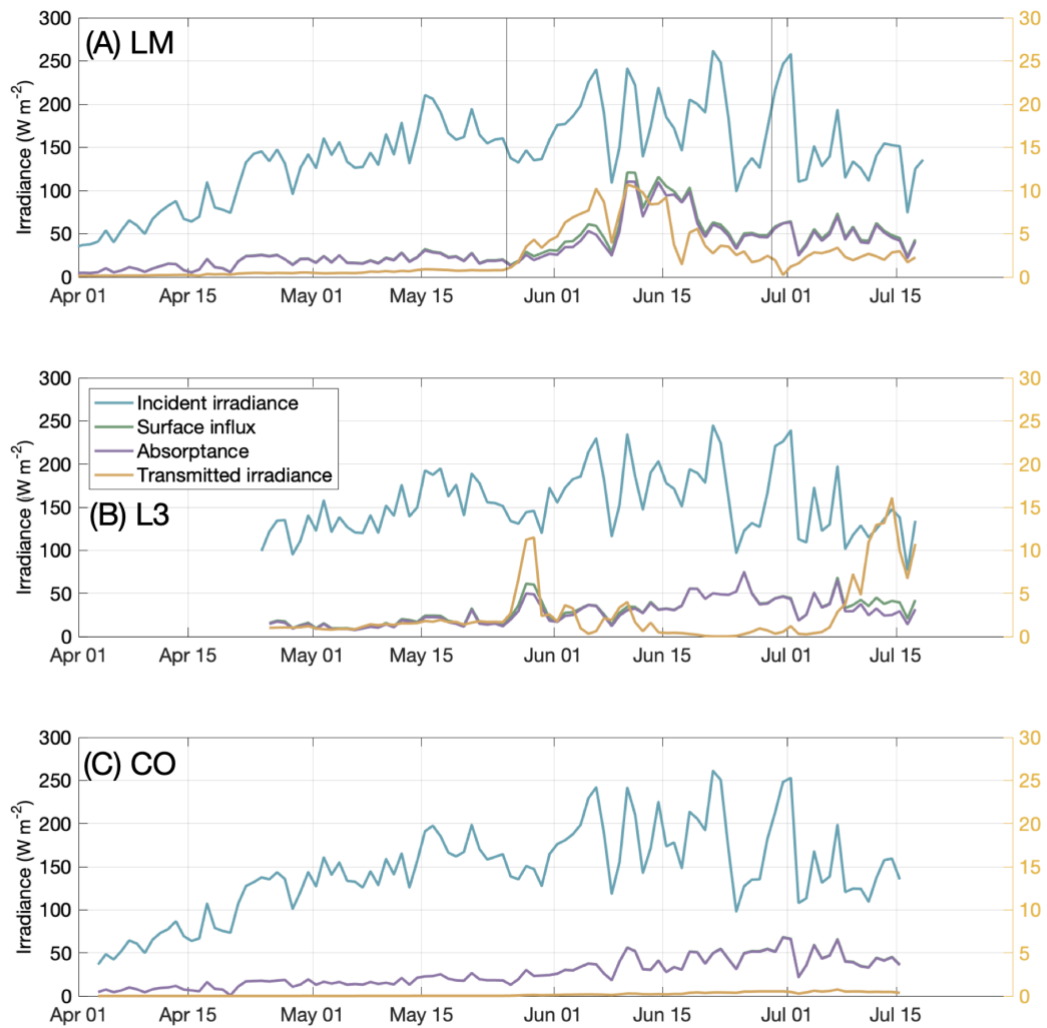
801



802

803 Figure 8. Transmittance spectra for selected dates in spring/summer 2020. (A) LM and (B) L3
 804 station. The solid vertical lines highlight the wavelengths of 440 nm and 600 nm, because of
 805 their relevance for the $\tau(600)/\tau(450)$ ratio (Figure 4F). In addition, the wavelength of 670
 806 nm is highlighted, representing the centre of absorption of Chlorophyll-a.

807



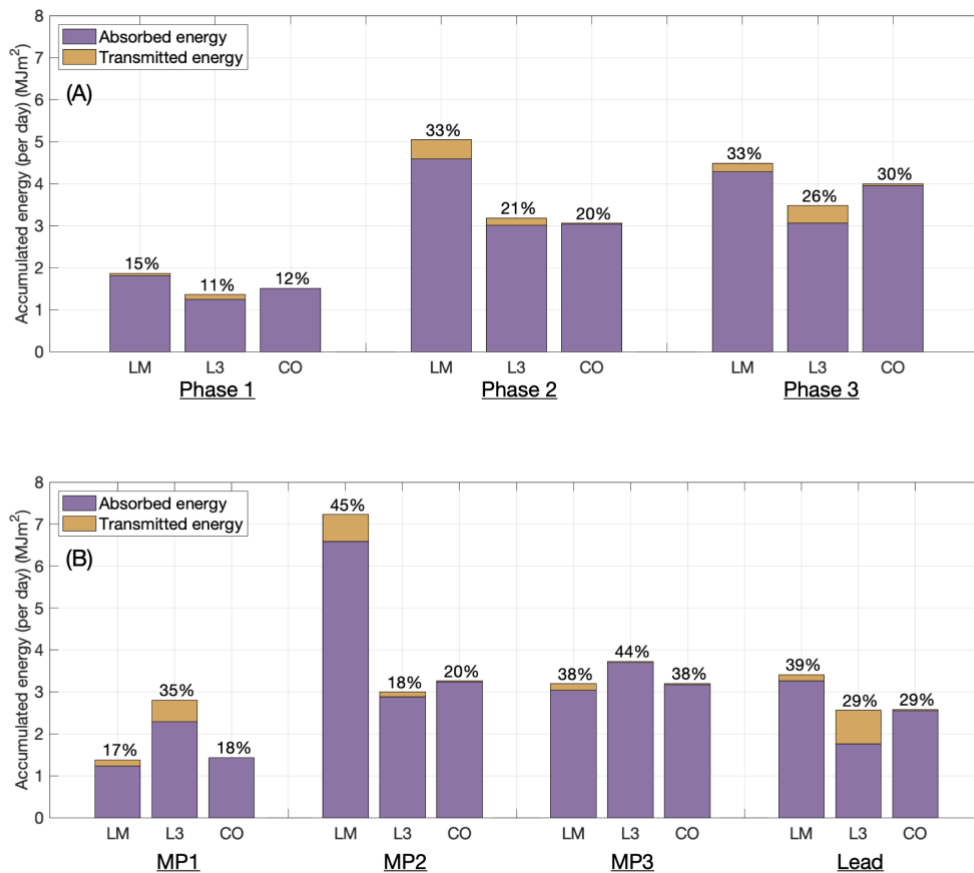
808

809 Figure 9. The seasonal evolution of the radiative fluxes of sea ice at different sites during
 810 spring/summer 2020. Daily mean of incident irradiance, flux into the surface, absorptance
 811 by sea ice plus the uppermost ocean, and transmitted irradiance into the ocean at (A) LM,
 812 (B) L3, and (C) CO. At panel A, the two black vertical lines indicated the melt onset (May
 813 26) and stage of advanced melt and the formation of surface weathered layer (June
 814 28).

815

816

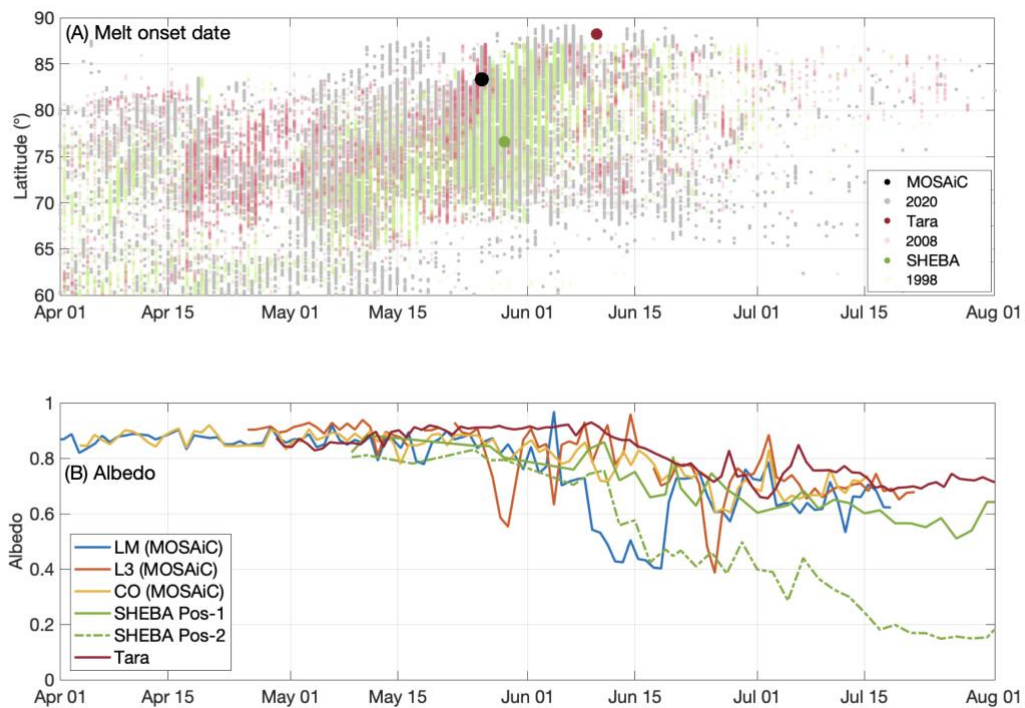
817



818

819 Figure 10. Daily mean of absorbed and transmitted irradiance at difference sites. (A)
 820 Integrated during Phase 1 (April 25 to May 26), Phase 2 (May 26 to June 29), and Phase 3
 821 (June 30 to July 15). (B) Integrated over individual events: MP1: first ponding event at L3 site
 822 (May 26 to May 29), MP2: ponding event at LM site (June 4 to June 19), MP3: second
 823 ponding event at L3 site (June 25 to June 29), and lead formation near the L3 site (July 10 to
 824 July 15). The text above each bar shows the ratio of the energy deposition (total of absorbed
 825 and transmitted) to the mean solar incoming energy during each phase and event.

826



827

828 Figure 11. Surface evolution and melt onset date. (A) Melt onset from the MOSAiC, Tara
 829 (Nicolaus et al., 2010), and SHEBA (Perovich et al., 2002) expeditions. The melt onset
 830 date is acquired from SMMR (Scanning Multichannel Microwave Radiometer) (Anderson et al.,
 831 2019). (B) albedo measurements from the MOSAiC, Tara (Nicolaus et al., 2010), and
 832 SHEBA (Perovich et al., 2002) expeditions when transitioning into the melt season. The
 833 SHEBA albedo is extracted as 2 fixed positions (Pos-1 and -2) from the albedo line
 834 observation.

835

836